

Hydromechanical coupling tests for mechanical and permeability characteristics of fractured limestone in complete stress–strain process

Yanlin Zhao^{1,2} · Jingzhou Tang¹ · Yu Chen³ · Lianyang Zhang⁴ · Weijun Wang¹ · Wen Wan¹ · Jianping Liao¹

Received: 29 June 2016 / Accepted: 5 December 2016 / Published online: 24 December 2016
© Springer-Verlag Berlin Heidelberg 2016

Abstract To clarify mechanical and permeability characteristics of fractured limestone in complete stress–strain process, the hydromechanical coupling tests with various differential water pressures and confining pressures were performed. The mechanical characteristics of fractured limestone specimens are sensitive to confining pressure, differential water pressure, and effective stress. The increasing differential water pressure weakens the rock strength and deformation modulus by activating the lateral deformation of fractured limestone, which is attributed to the decrease in the effective minimum principal stress. The experimental results verify the validity of Mohr–Coulomb yield criterion considering the effective stress effect under hydromechanical coupling condition. The permeability values display four stages of decrease–gradual increase–rapid increase–small drop in complete stress–strain process, which roughly correspond to volumetric compression stage, elastic deformation stage, yield, and post-peak stage,

as well as residual strength stage, respectively. At a low differential water pressure in the range of 2–5 MPa, the corresponding relationship mentioned above is obvious. However, at high differential water pressures up to 8–14 MPa, there is a deviation from the correspondence above, i.e., permeability reduction stage is shorter than the stage of volumetric compression. A cubic polynomial is used to describe the relationship between permeability and volumetric strain at volumetric compression stage. However, it is difficult to describe the relationship between the permeability and volumetric strain by a uniform fitting equation at the dilatancy stage.

Keywords Hydromechanical coupling · Fractured limestone · Permeability · Strength · Deformation · Complete stress–strain process

Introduction

Permeability of rocks has been widely assumed to be one type of rock properties. However, it is more like a “process” than a “material property” because it is closely related with the stress–strain conditions of rocks (Heiland 2003; Wang et al. 2013).

The weakening effect of water on the rock strength has been revealed in some experimental research (Lajtai et al. 1987; Masuda 2001), and it is closely related to the mineral composition and the water content (Vásárhelyia and Ván 2006). In addition, if the rock is subjected to differential water pressure, the weakening effect on mechanical characteristics may become more complicated (Li et al. 2013). The seepage behavior of water in rock reduces the effective confining pressure, resulting in a decrease in rock strength and an increase in deformation. However, the definite

✉ Yanlin Zhao
yanlin_8@163.com

✉ Yu Chen
yu.chen@csu.edu.cn

¹ Hunan Provincial Key Laboratory of Safe Mining Techniques of Coal Mines, Work Safety Key Laboratory on Prevention and Control of Gas and Roof Disasters for Southern Coal Mines, Hunan University of Science and Technology, Xiangtan 411201, Hunan, China

² State Key Laboratory of Coal Resources and Safety Mining, China University of Mining and Technology, Xuzhou 221008, Jiangsu, China

³ School of Resources and Safety Engineering, Central South University, Changsha 410083, China

⁴ Department of Civil Engineering and Engineering Mechanics, University of Arizona, Tucson, AZ 85721, USA

relationship among strength, deformation of rock and differential water pressure was still unknown, due to the variability of porosity and cracks structure and mineral composition of rocks. Since the principle of effective stress was pioneered by Von Terzaghi (1923), various effective stress principles were proposed for porous and fractured media (e.g., Tuncay and Corapcioglu 1995; Laloui and Nuth 2009; Ghabezloo et al. 2009; Xie and Shao 2015; Li et al. 2016). The development of the effective stress models enhances the understanding on the hydromechanical coupling behaviors of soils and rock fractures. For fractured rock, however, few experimental efforts were made to examine the validity of strength yield criterion considering the effective stress effect.

The permeability of rock is as important as the mechanical characteristics under the hydromechanical coupling condition. It is well understood that in complete compressive stress–strain process, the rock experiences several stages including initial compression, quasi-linear deformation, non-linear deformation, failure up to a peak strength and a strain-softening period. The compression may lead to the reduction of permeability as a result of pores and cracks closure. Conversely, the growth and coalescence of micro-cracks during the loading process may result in the enhancement of the permeability. In order to establish the correlation between the stress–strain and the permeability, many experiments have been conducted (e.g., Zoback and Byerlee 1975; Bai et al. 1999; Suri et al. 1997). The relationship between the stress–strain and the rock failure mechanism have also been investigated by many researchers (e.g., Barton et al. 1985; Li et al. 1994; Zhu and Wong 1997; David et al. 2001; Heiland 2003; Olivella et al. 2004; Shao et al. 2005; Zhang et al. 2013). These investigations have indicated that the stress–strain process of rock has an obvious effect on the permeability, and some kinds of functions were used to describe the relationship between the strain and the permeability (Gangim 1978; Tsang and Witherspoon 1981; Hicks et al. 1996; Shan et al. 2000; Zhang et al. 2007; Konecny and Kozusnikova 2011; Wang and Xu 2013). For example, Li et al. (1994, 1997) investigated the permeability of Yinzhuang sandstone with respect to a complete stress–strain path. It was found that the polynomial permeability–strain equations are appropriate to fit the experimental data of permeability versus axial strain. To better reflect the permeability at the stage of post-peak, Wang and Xu (2013) proposed two kinds of empirical equations which are fitted to better describe the relationship between the permeability at the stages of compression and dilatancy.

Although extensive research has been carried out on the stress–strain and permeability behavior of rock, the previous studies mainly focused on intact rocks, instead of fractured rocks. Those studies generally adopted the

transient pulse method to measure permeability of rock, rather than the steady-state method. (Li et al. 1994; Zhu and Wong 1997; David et al. 2001; Heiland 2003). Since water flows mainly through along rock fractures, it is more meaningful to study the mechanical and permeability characteristics of fractured rock in complete stress–strain process subjected to various confining pressures and water pressures. Moreover, it is especially necessary to study the effect of differential water pressure and effective stress on the mechanical behaviors of fractured rock due to the lacking of previous investigations.

Maokou limestone is one common type of rocks in southern China. So far, numbers of highway tunnels have to be built in Maokou limestone stratum. The worst case is that the water-bearing karst caves generally exist in such stratum. During the excavation process of tunnels, once karst caves are encountered, the confined karst cave water may break through the surrounding rock masses and erupt due to hydromechanical coupling effect. Thus, it is of vital importance to evaluate the mechanical and permeability characteristics of fractured Maokou limestone in complete stress–strain process under hydromechanical coupling condition.

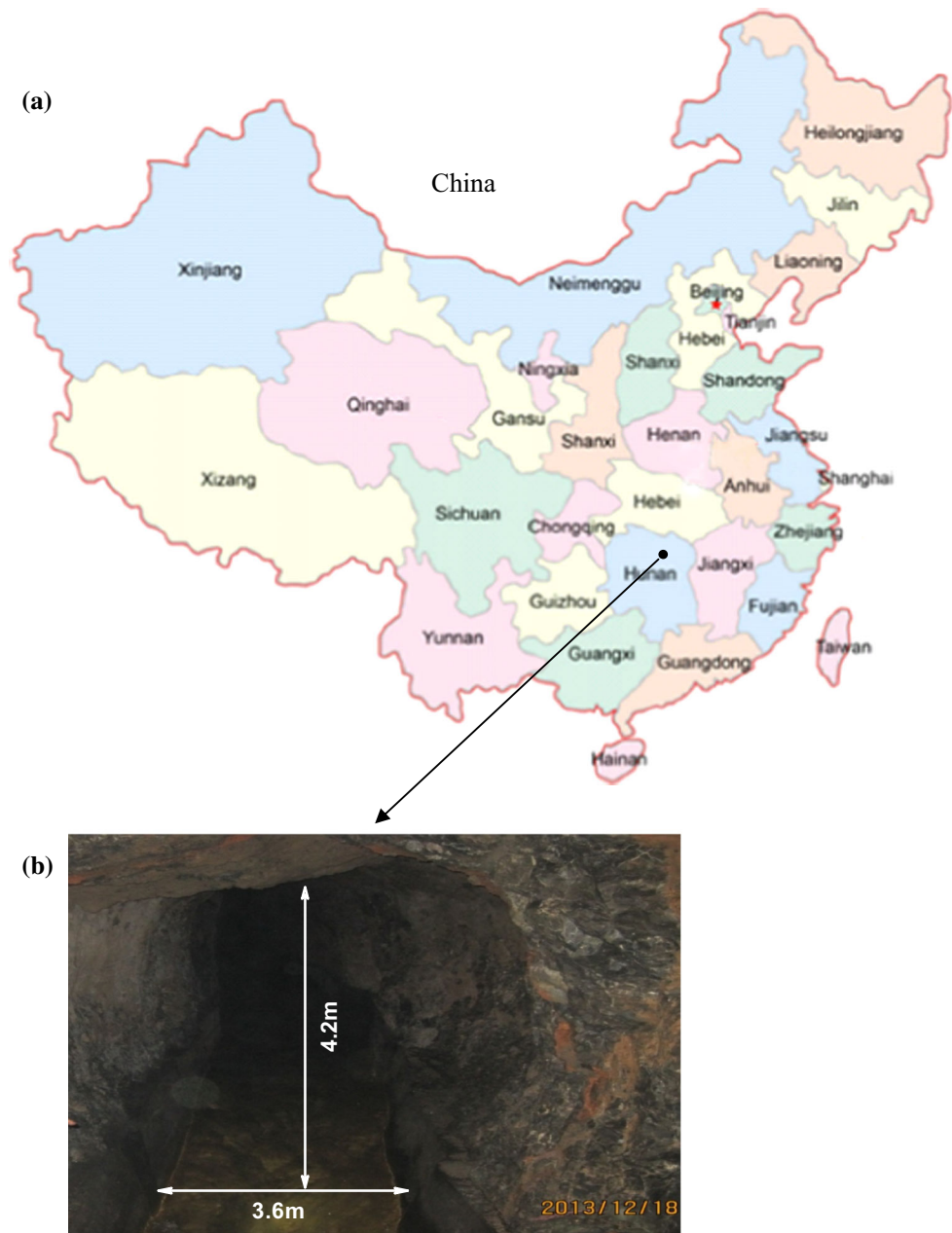
The objective of this study is to investigate the mechanical and permeability characteristics of fractured Maokou limestone in complete stress–strain process by using steady-state method, as well as to clarify the hydromechanical coupling effect of fractured limestone at various confining pressures and differential water pressures.

Test methodology

Specimen preparation and porosity measurement

The 100-mm-diameter core specimens of Maokou limestone were taken from an underground roadway construction site at the Meitanba highway tunnel located in south China. Figure 1a, b illustrates the map showing the location of sample point and surrounding rock of the sampling site, respectively, where the rock mass is moist and contains many fractures. The specimens were cut into lengths of 202 mm and then ground to 200 mm to ensure that the two surfaces were parallel to each other in accordance with the specifications recommended by the International Society for Rock Mechanics (ISRM). Some fractured limestone specimens containing multiple irregular intermittent cracks (Fig. 2) were preliminarily chosen from all rock cores to perform permeability tests in complete stress–strain process. Based on X-ray diffractometer (XRD) analysis, the tested fractured limestone is mainly composed of calcite (83%), dolomite (10%), micas and shales (5%), and quartz (2%). The degree of preexisting fractures in a specimen

Fig. 1 a A map showing the location of sample point, and **b** surrounding rock of the sampling site (underground roadway at a depth of 510 m)



was determined based on the measured P-wave velocity of the specimen prior to testing. The P-wave velocity was measured along four different diametrical directions and along the specimen height direction and the average of the measured values was used afterward. Thirty-two fractured limestone specimens with P-wave velocity in range from 1.8 to 2.2 km/s were ultimately used as the tested specimens. The developments and orientations of intermittent fractures with length ranges of 5.0–50.0 mm are analyzed statistically for each specimen. The statistical results indicate that the average linear density of fracture along axial direction is 47.5/m, and the average angle between the fracture and axial direction is 43.1°.

Specimens were dried for 72 h at $T = 50\text{ }^{\circ}\text{C}$, and then saturated by using de-ionized water under vacuum for 48 h prior to experiments. Initial porosity was calculated as

$$\phi = \frac{V_V}{V_0} \tag{1}$$

where V_v is the volume of voids, derived by the difference in weight between the dry and saturated specimen, and V_0 is the initial total volume.

Based on the measured difference in weight between the dry and saturated specimens, the porosity of tested specimens ranged from 12 to 16%, according to Eq. (1).

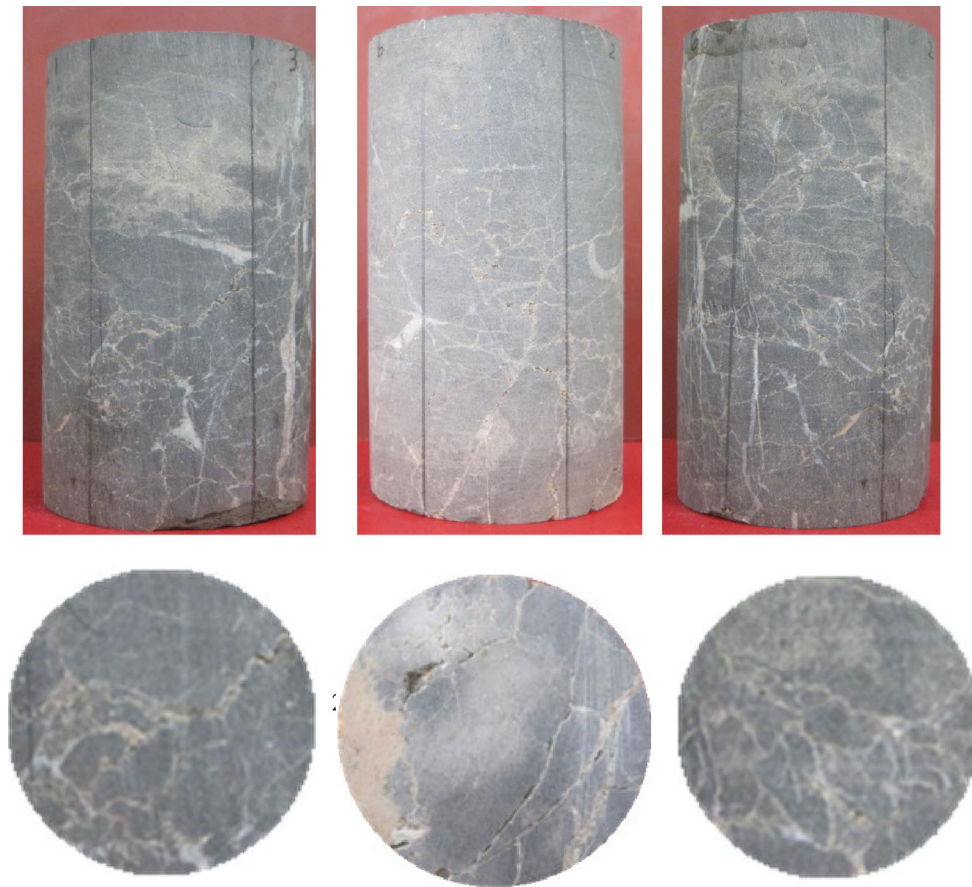


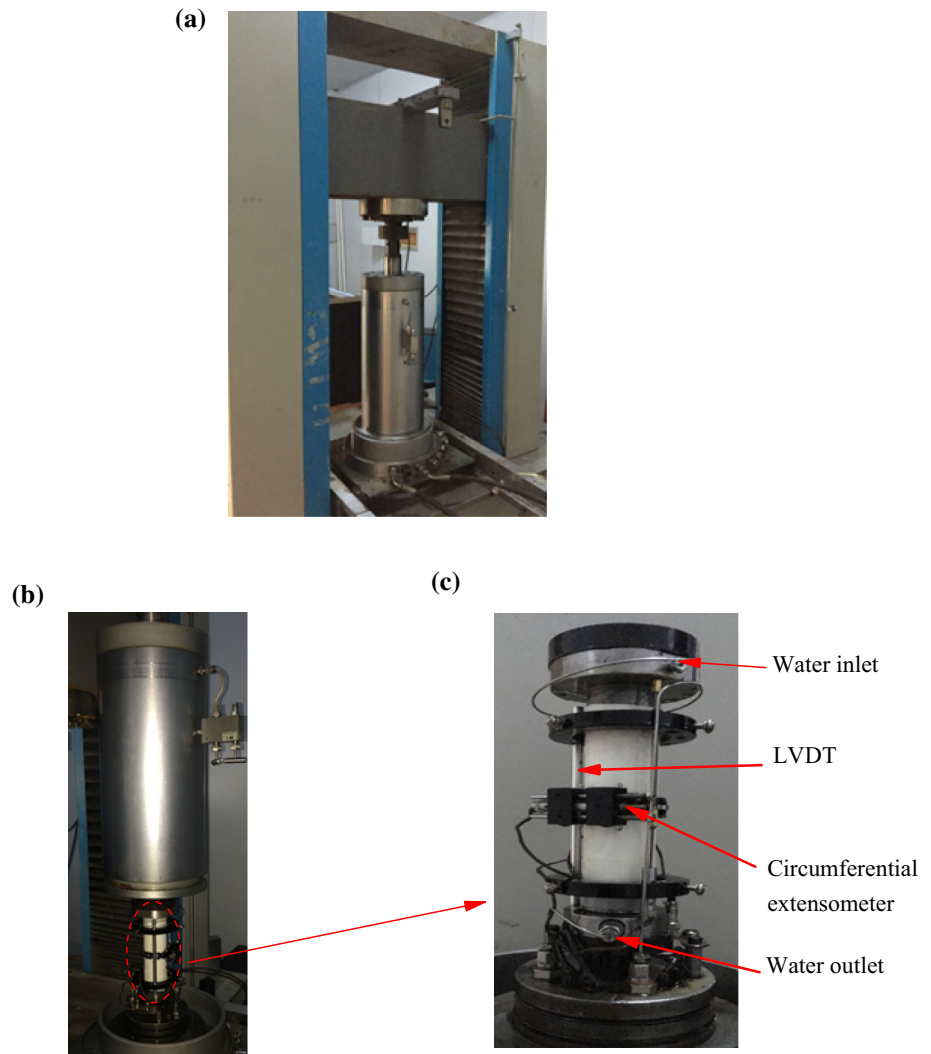
Fig. 2 Some fractured limestone specimens

Experimental setup and procedure

The permeability of fractured limestone was measured by using steady-state flow method. Permeability tests were performed by using the high-pressure hydromechanical coupled test setup (TAW-2000) in the rock mechanics laboratory at Hunan University of Science and Technology in China. The capacities of such test rig (see Fig. 3a) are 60 MPa for fluid pressure, 70 MPa for confining pressure and 2000 kN for axial load. Due to the auto-compensation system, the axial force is entirely transmitted as deviatoric stress. Initially, the saturated specimen was circumferentially sealed in shrinkable plastic sleeve and mounted with both axial and circumferential deformation measurement devices. The axial deformation was measured with a pair of LVDTs (linear variable displacement transducer), and the lateral deformation with a circumferential extensometer connected to a roller chain assembly wrapped around the jacketed specimen in mid-height of the specimen (see Fig. 3b, c). The volumetric strain ε_v was calculated by the summation of the axial (ε_1) and lateral (ε_3) strains (i.e., $\varepsilon_v = \varepsilon_1 + 2\varepsilon_3$). The assembled specimen was placed into the chamber on pedestal of the load frame (Fig. 3b). After

placing the specimen, the confining pressure induced by hydraulic oil was gradually increased to required value, and the axial stress was kept on the same value as a confining pressure so that a hydrostatic three-dimensional stress status was initially induced in the specimen ($\sigma_1 = \sigma_2 = \sigma_3$). Afterward the fluid pressure was increased to a predetermined value which was smaller than confining pressure to avoid leakage. The inlet water pressure was applied on the upstream end of the specimen, and outlet was open to the atmosphere. During the water permeability measurement test, the inlet water pressure was kept constant by a servo-control. The outlet volumetric water flow rate at the downstream end of the specimen was measured in real time by Alicat L-Series Water Flow Meters, with available range of 0.5 CCM to 10 LPM and $\pm 2\%$ accuracy of full scale in calibration conditions at a sampling interval of 1.0 s. During permeability tests, firstly, the initial permeability under hydrostatic conditions was measured prior to the deviatoric stress conditions. After the initial permeability was determined, at constant confining pressure, the axial loading was applied as smoothly as possible at a very low axial strain ratio value of $3 \times 10^{-6} \text{ s}^{-1}$ to avoid a strong transient disturbance of the flow rates during the

Fig. 3 **a** High-pressure hydromechanical coupled test setup (TAW-2000), **b** the location of specimen with sensors in triaxial cell, and **c** deformation sensor measurement system



axial loading, then a lateral deformation rate of 0.05 mm/min was maintained after the yield stress shown up. During continuously deforming the specimen at very low strain rate, the flow rate through specimen was measured at constant inlet water pressure. At the same time, axial load, axial strain, lateral strain, and confining pressure were measured at a sampling interval of 1.0 s.

For steady-state flow method, based on the classic Darcy’s law, the permeability can be calculated from the measured differential water pressure and flow rate.

$$K = \frac{Q\mu L}{A\Delta p_w} \tag{2}$$

where K is the permeability; Q is the constant influx of fluid; μ is the dynamic viscosity of the fluid; L is the length of the specimen; Δp_w is the differential water pressure; and A is the cross-sectional area of the specimen.

To study mechanical and permeability characteristics of fractured limestone subjected to various differential water pressures and confining pressures, the differential water

pressures applied on specimens were set to 2, 5 (relatively lower values), 8, 11, and 14 MPa (relatively higher values), respectively, as well as the confining pressures were set to 7, 12, 17, and 22 MPa, respectively. In order to accurately compare experimental results, the same loading procedure was performed to all experiments with the test duration range of 40–50 min for each specimen.

Two specimens were tested at each combination of differential water and confining pressures. Therefore, the 32 specimens were used to test the mechanical and permeability characteristics of fractured limestone.

Results and analyses

Mechanical characteristics

To study the influence of the confining pressure and differential water pressure on the deformation of fractured limestone, the deformation modulus E_{50} and Poisson’s ratio

μ at the 50% of the peak differential strength were calculated as (Meng et al. 2012)

$$E_{50} = \frac{\sigma_1 - 2\mu\sigma_3}{\varepsilon_1} \tag{3}$$

$$\mu = \frac{B\sigma_1 - \sigma_3}{(2B - 1)\sigma_3 - \sigma_1} \tag{4}$$

$$B = \frac{\varepsilon_3}{\varepsilon_1} \tag{5}$$

where σ_1 and σ_3 are the axial stress and confining pressure at the 50% of the peak differential strength, respectively; ε_1 and ε_3 are the axial and lateral strains at the 50% of the peak differential strength, respectively.

The experimental results on mechanical parameters of fractured limestone subjected to various confining pressures and differential water pressures are listed in Table 1. Taking the confining pressures of 7, 12, 17, and 22 MPa for example, the curves of stress and axial and volumetric strains at different confining pressures and differential water pressures are presented in Figs. 4 and 5. The stress–axial strain curves show the similar characteristics. An initial phase of micro-cracks and pores compression is followed by quasi-linear compaction. With continued loading, the departure from quasi-linear behavior indicates macroscopic specimen yielding and a peak stress is reached followed by a stress drop. Deformation continues until a residual strength is attained. The typical stress–volumetric strain curve is shown in Fig. 6 (Baud et al. 2000). The volumetric strain is characterized by an initial phase of

compaction-dominated behavior followed by a phase of dilatancy-dominated behavior. When the rock deforms, the compaction-dominated stage occurs initially in which the positive volumetric strain increases gradually until the maximum positive volumetric strain appears. Afterward, a turn point (Point B) shows up, where the deformation of the specimen switches from compaction-dominated to dilatancy-dominated. As the stress increases further, more and more micro-cracks occur, and the specimen continues dilating. The volumetric strain eventually passes through zero volumetric strain (Point D) before it continues to increase until specimen fails.

The stress–axial strain curves (Fig. 4) demonstrate an increase in confining pressure contributes to the increase in the peak and residual strengths at the same differential water pressure. Moreover, in all cases, the failure mode remains brittle even at the highest confining pressure of 22 MPa (i.e., the capability of the rock to resist load drop with permanent strain, see Rutter 1986).

The influence of the confining pressure on deformation modulus E_{50} and Poisson’s ratio μ at the 50% of the peak strength is obvious as shown Figs. 7a, b. It can be seen that E_{50} increases nonlinearly with the increasing confining pressure, p_c , and the relationship between E_{50} and p_c can be described by a logarithmic equation below

$$E_{50} = \alpha \ln p_c + \beta \quad (p_c \geq \Delta p_w) \tag{6}$$

where α , β are fitting parameters. The fitting curves and equations were both depicted in Fig. 7a for the tested specimens in a semilogarithmic scale.

Table 1 Basic mechanical parameters obtained from hydromechanical coupling experiments at various confining and differential water pressures

Differential water pressure (MPa)	Confining pressure (MPa)	Peak differential strength (MPa)	E_{50} (GPa)	Poisson’s ratio	Residual differential strength (MPa)
2	7	60.6	25.4	0.32	31.6
	12	75.8	31.1	0.30	52.8
	17	82.4	35.4	0.21	66.0
	22	98.3	39.2	0.17	87.2
5	7	42.0	16.0	0.38	24.7
	12	68.4	27.3	0.31	44.2
	17	77.6	32.0	0.22	54.9
	22	95.2	36.1	0.20	80.7
8	12	60.0	21.3	0.30	36.1
	17	75.6	25.5	0.26	49.2
	22	88.5	34.0	0.25	72.8
11	12	54.0	17.2	0.35	30.6
	17	70.4	23.2	0.24	43.8
	22	85.6	27.9	0.27	60.9
14	17	64.1	20.9	0.29	34.9
	22	78.2	26.3	0.31	57.2

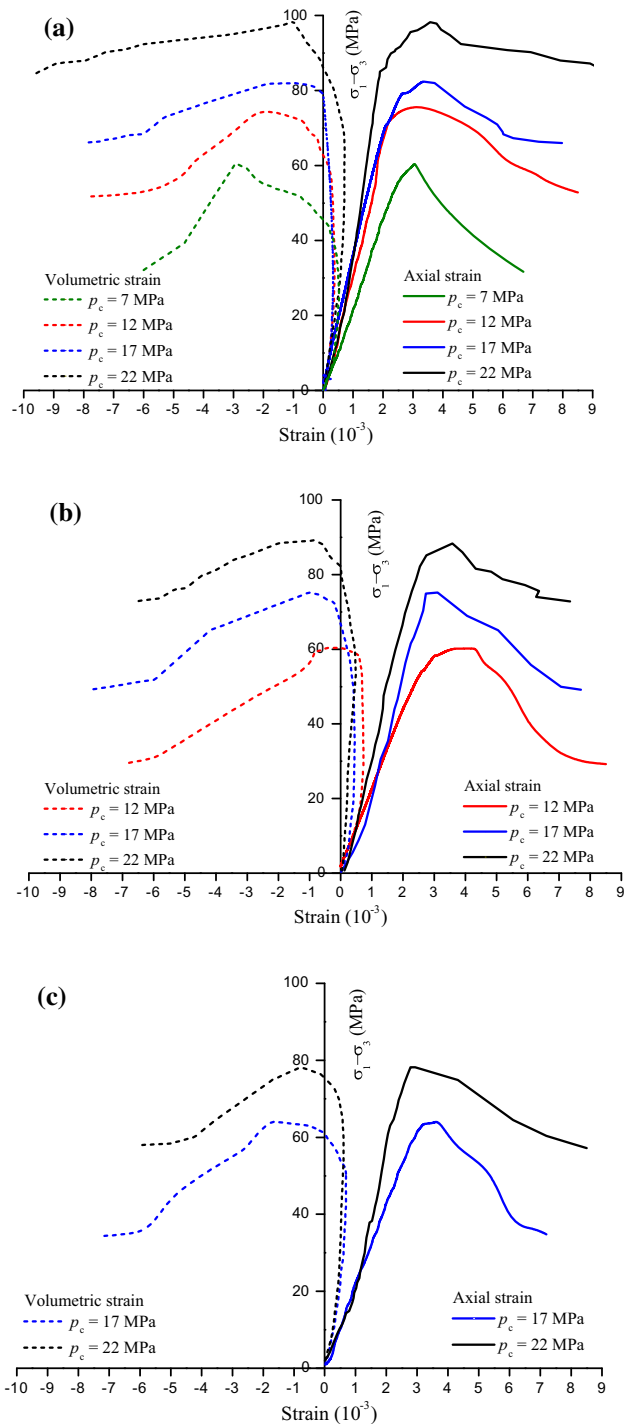


Fig. 4 Curves of stress–axial, volumetric strains at differential water pressures of **a** 2 MPa, **b** 8 MPa, and **c** 14 MPa

Poisson’s ratio μ follows a decreasing trend as the confining pressure increases at the same differential water pressure with two exceptions that when $\Delta p_w = 11$ MPa, $p_c = 17$ MPa, and $\Delta p_w = 14$ MPa, $p_c = 17$ MPa as illustrated in Fig. 7b.

The effect of differential water pressure, Δp_w on mechanical characteristics of fractured limestone is significant. Figure 5 presents the curves of stress and axial and volumetric strains at a variety of differential water pressures under the same confining pressure. In Fig. 5, the slope and peak of the curves both reduce with the increasing differential water pressure, which indicates the water pressure has not only obvious strengthening effect on the deformation of specimen but also a weakening effect on strength of specimen. The experimental data of E_{50} versus Δp_w , and μ versus Δp_w for the tested specimens are illustrated in Figs. 8a, b. From Fig. 8a, it can be found that E_{50} reduces with the increasing differential water pressure, Δp_w , and an approximate linear relationship between E_{50} and Δp_w at the same confining pressure can be observed

$$E_{50} = \lambda \Delta p_w + \gamma \quad (\Delta p_w \leq p_c) \tag{7}$$

where, λ , γ are fitting parameters. The fitting curves and equations were both depicted in Fig. 8a for the tested specimens. The fitting equations are in good agreement with the experimental data with an average correlation coefficient of 0.941. Figure 8b shows the obvious effect of differential water pressure, Δp_w , on Poisson’s ratio μ . In general, μ increases with the greater differential water pressure, Δp_w .

Under conventional triaxial state, the effective axial stress σ'_1 is calculated as the difference between the applied axial stress σ_1 and pore fluid pressure p_w ($\sigma'_1 = \sigma_1 - p_w$). Similarly, the effective confining pressure p'_c acting on the specimen is calculated as the difference between the confining and pore pressures ($p'_c = p_c - p_w = \sigma'_2 = \sigma'_3$) (Hubbert and Rubey 1959). For triaxial loading tests, where σ'_1 exceeds p'_c , the effective differential stress (σ'_d) is calculated as the difference between effective axial stress and effective confining pressure (i.e. $\sigma'_d = \sigma'_1 - \sigma'_3 = (\sigma_1 - p_w) - (p_c - p_w) = \sigma_1 - p_c$). Therefore, the effective differential stress is independent of pore fluid pressure. For the constant flow method in present tests, the effective confining pressure, p'_c can be calculated as

$$p'_c = p_c - \frac{1}{2} \Delta p_w \tag{8}$$

Under conventional triaxial test, the effective minimum principal stress, σ'_3 , equals the effective confining pressure, p'_c . The experimental data of E_{50} and μ versus σ'_3 are illustrated in Fig. 9a, b, respectively. E_{50} approximately increases linearly with the increasing effective minimum principal stress, σ'_3 at the same confining pressure. Both the fitting curves and equations are depicted in Fig. 9a. The fitting equations are in good agreement with the

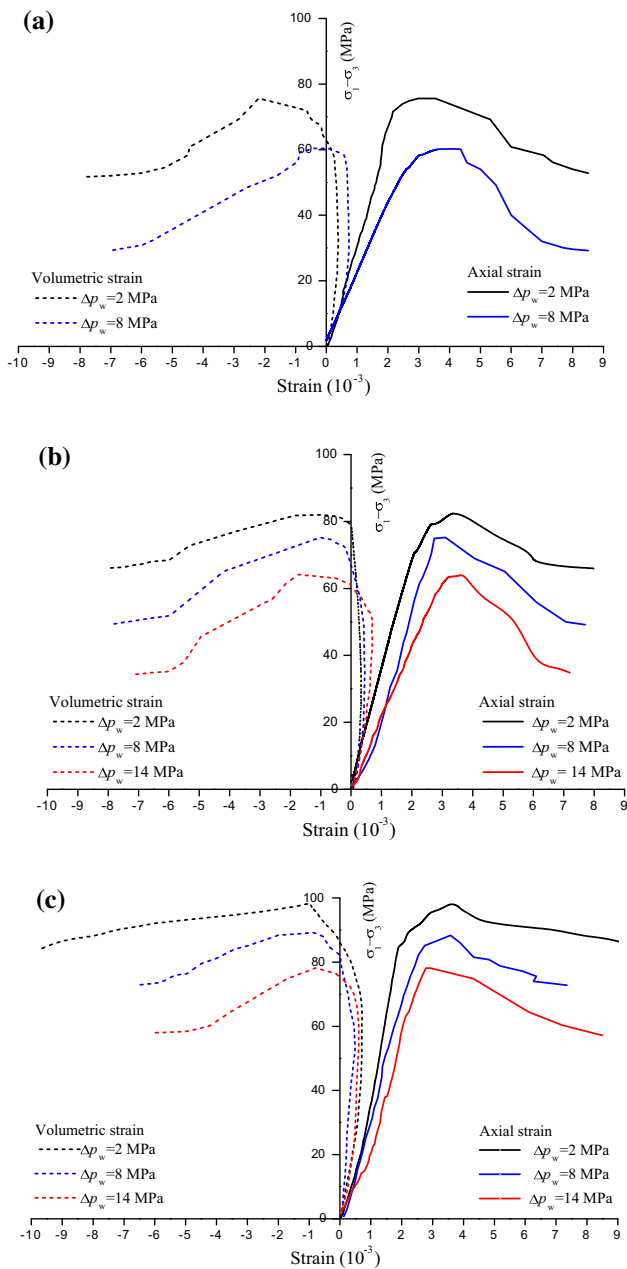


Fig. 5 Curves of stress–axial, volumetric strains at confining pressure of **a** 12 MPa, **b** 17 MPa; and **c** 22 MPa

experimental data with an average correlation coefficient of 0.964. In general, μ decreases with the increase in the effective minimum principal stress, σ'_3 as depicted in Fig. 9b. By comparing Fig. 8a, b with Fig. 9a, b, it can be observed that the effect of the increasing differential water pressure on mechanical characteristics of fractured limestone is essentially the same as the effect of the decreasing effective minimum principal stress.

The variation laws of the effective differential strength, S'_d with the effective minimum principal stress, σ'_3 for the

tested specimens were depicted in Fig. 10. A linear equation can be performed well to fit the relationship between S'_d and σ'_3 .

$$S'_d = k\sigma'_3 + d \tag{9}$$

where k and d are fitting parameters, respectively. The fitting curves of experimental data are depicted in Fig. 10. The linear fitting equation with $k = 3.18$, and $d = 35.1$ is in good agreement with the experimental data with a correlation coefficient R^2 of 0.921.

According to Mohr–Coulomb yield criterion, the relationship between the effective differential strength, S'_d , and the effective minimum principal stress, σ'_3 , is expressed as

$$S'_d = \left(\frac{1 + \sin \phi'}{1 - \sin \phi'} - 1 \right) \sigma'_3 + \frac{2c' \cos \phi'}{1 - \sin \phi'} \tag{10}$$

Based on Eqs. (8)–(10), effective cohesion $c' = 8.59$ MPa, and effective friction angle $\phi' = 37.9^\circ$. It indicates that the unified effective strength parameters (c' and ϕ') can be obtained in Mohr–Coulomb yield criterion under hydromechanical coupling condition. The experimental results of fractured limestone confirm the validity of Mohr–Coulomb yield criterion under hydromechanical coupling condition.

Relationships between axial strain and permeability

During testing, axial strain, lateral strain, and outlet flow were measured by using LVDTs, circumferential extensometer and Alicat L-Series Water Flow Meters, respectively. Experimental results indicate that the outlet flow values are in the range of 14.5 mL/min–8.64 L/min in complete stress–strain process for all specimens. The representative permeability–strain experimental curves of fractured limestone in complete stress–strain process are plotted in Fig. 11 in accordance with the stress–strain curves.

The permeability evolution of fractured limestone specimen in the complete stress–strain process shows a logical feature and can be divided into several phases (Martin and Chandler 1994). At the first phase of compression (region OA), the initial micro-cracks and pores within the rock specimens are compressed to closure and the permeability gradually decreases with the increase in the stress and strain. At the second phase of quasi-elastic deformation (region AE) of the complete stress–strain curve, the first structural damage appears randomly as elongated non-interconnected micro-cracks (Jaeger and Cook 1979), which causes permeability to increase slightly as the rock begins to dilate. As the axial stress increases at this stage, the permeability increases until the yield stage is reached (Point E), in which the stress–strain curve deviates

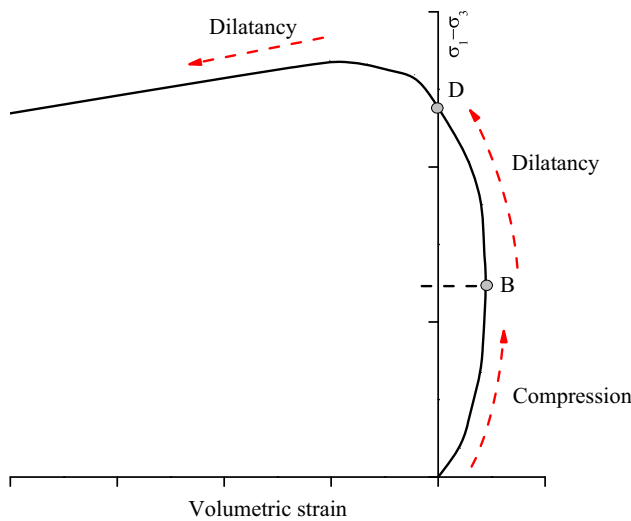


Fig. 6 Typical stress–volumetric strain curve

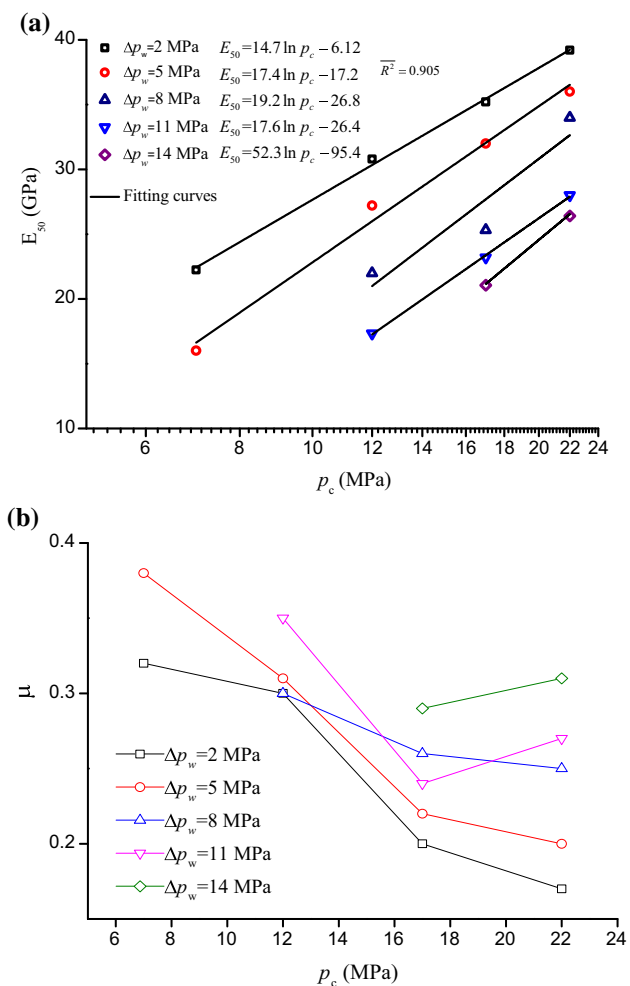


Fig. 7 **a** E_{50} versus p_c , and **b** μ versus p_c at various differential water pressures

from the straight line and dive downward and the slope of the curves decreases gradually. The yield stage corresponds to a significant increase in permeability due to the nucleation and growth of micro-cracks. When the peak strength is reached at point F, a macroscopic fracture plane develops, which causes a jump in permeability. After peak strength is reached, the permeability continues to increase before reaching its peak value at point G. In most cases, the maximum permeability occurs within the strain-softening period. Rock failure and the maximum permeability do not coincide, whereas the further development of deformation after rock failure brings the occurrence of peak permeability. After the maximum permeability at post-peak stage shows up, the permeability is determined by the properties of the shear band especially. Continuous straining results in frictional sliding on shear band, and permeability usually follows a slight drop with some fluctuations as the post-peak strain develops. The experimental results of permeability characteristics of fractured limestone in a complete stress–strain process agree with the previous findings (Li et al. 1994, 1997; Wang and Park 2002; Schulze et al. 2001; Heiland 2003; Wang et al. 2013).

For the convenience of analysis, the six key permeability values below can be selected from the experimental data following these definitions: (1) the initial permeability (K_0) under hydrostatic pressure; (2) the minimum permeability (K_{min}) among all test points; (3) the permeability (K_c) of maximum volumetric compression point; (4) the permeability (K_z) of zero volumetric strain; (5) the permeability (K_s) of the peak stress point; (6) the maximum permeability (K_{max}) among all test points.

The experimental data of six key permeability values at various differential water pressures and confining pressures are listed in Table 2. According to Table 2, the evolution of six key permeability values is different at various differential water pressures. To comparatively investigate the evolution laws, taking a confining pressure of 17 MPa and differential water pressures of 2, 8, 14 MPa for example, the permeability–axial strain curves in complete stress–strain process are plotted in Figs. 12, 13, and 14, respectively.

For a differential water pressure of 2 MPa under confining pressure of 17 MPa, in the permeability–strain curves (Fig. 12), the closure of existing cracks and grain boundaries leads to a decrease in permeability during compaction. Compared with the initial permeability K_0 ($K_0 = 1.47 \times 10^{-16} \text{ m}^2$), the permeability K_c ($K_c = 7.10 \times 10^{-15} \text{ m}^2$) of maximum volumetric compression point decreases 52% from original value, which is very close to the minimum permeability K_{min} ($K_{min} = 6.01 \times 10^{-15} \text{ m}^2$). When dilatancy starts to dominate the deformation regime, the nucleation and growth of micro-cracks result in a gradual increase in permeability.

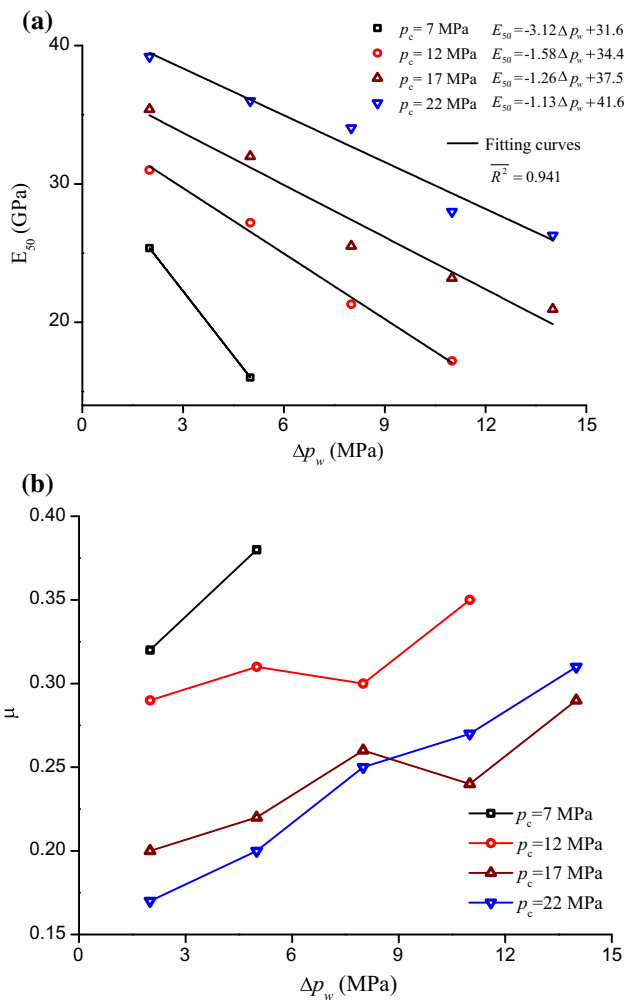


Fig. 8 **a** E_{50} versus Δp_w , and **b** μ versus Δp_w at various confining pressures

However, the permeability K_z ($K_z = 1.20 \times 10^{-16} \text{ m}^2$) of zero volumetric strain still do not reach initial permeability K_0 . As dilatancy further develops, brittle failure is reached and the permeability $K_s = 3.37 \times 10^{-16} \text{ m}^2$, which is 2.29 times the initial one. At the post-peak stage, characterized by strain softening, a maximum permeability K_{\max} ($K_{\max} = 1.09 \times 10^{-15} \text{ m}^2$) occurs and it is 7.41 times the initial one, followed by a small permeability drop due to the frictional sliding on shear band. The order of permeability values is $K_{\min} \approx K_c < K_z < K_0 < K_s < K_{\max}$ at a differential water pressure of 2 MPa under confining pressure of 17 MPa.

In the permeability–strain curves at a differential water pressure of 8 MPa under confining pressure of 17 MPa (Fig. 13), during compaction, the minimum permeability K_{\min} ($K_{\min} = 2.47 \times 10^{-16} \text{ m}^2$) first occurs. It is about 59.1% of the initial permeability K_0 ($K_0 = 4.18 \times 10^{-16} \text{ m}^2$) and, even the volume continues to be compressed, the permeability changes to gradual increase. The permeability K_c of maximum

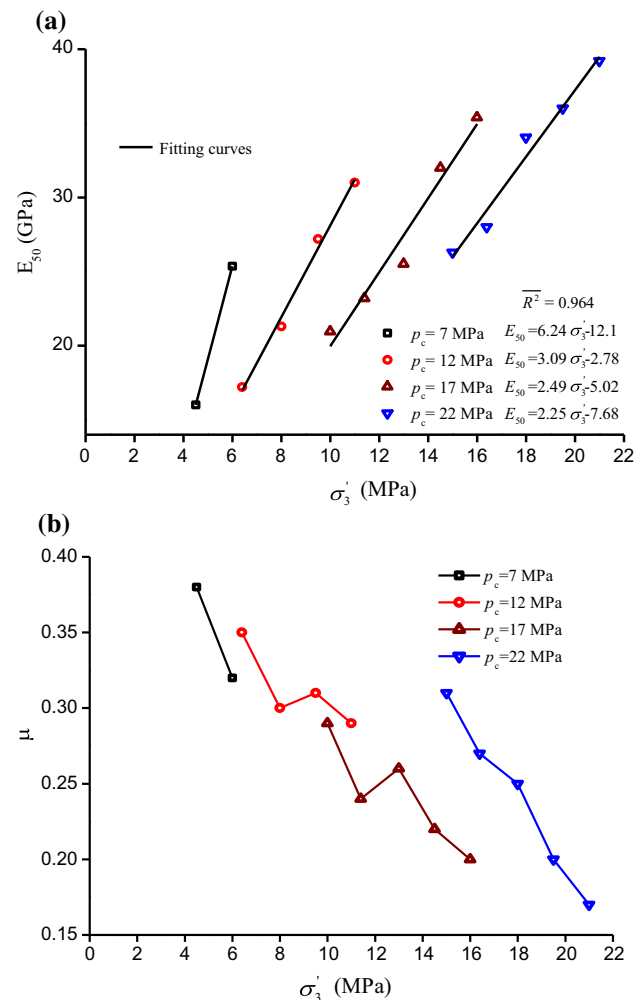


Fig. 9 **a** E_{50} versus σ_3 , and **b** μ versus σ_3 at various confining pressures

volumetric compression point, which value is $3.39 \times 10^{-16} \text{ m}^2$, is greater than the minimum permeability. When the volume dilates to zero, the permeability K_z ($K_z = 5.64 \times 10^{-16} \text{ m}^2$) is greater than the initial one. At peak stress point, the permeability K_s reaches $7.61 \times 10^{-16} \text{ m}^2$ which is 1.82 times the initial permeability. At the post-peak stage, the measurable maximum permeability K_{\max} is $2.36 \times 10^{-15} \text{ m}^2$ which is 5.65 times the initial permeability. The order of permeability values at a differential water pressure of 8 MPa under confining pressure of 17 MPa is: $K_{\min} < K_c < K_0 < K_z < K_s < K_{\max}$.

In the permeability–strain curves at a differential water pressure of 14 MPa under confining pressure of 17 MPa (Fig. 14), during axial loading, the first stage of the permeability drop is not noticeable, and the drop is only 6.19% of the initial permeability K_0 ($K_0 = 1.13 \times 10^{-15} \text{ m}^2$). After very transient and small drop, the permeability increases with the rising axial stress and strain. The permeability values of maximum volumetric compression

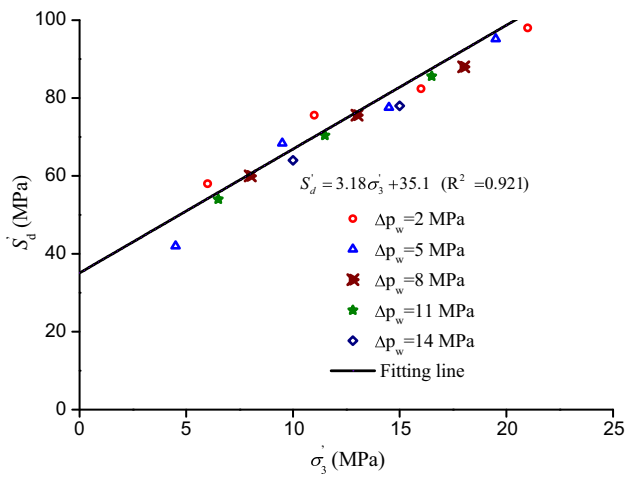


Fig. 10 S'_d versus σ'_3 under hydromechanical coupling condition for all specimens

point (K_c), zero volumetric strain point (K_z), peak stress point (K_s), and maximum permeability (K_{max}) at post-peak stage are 1.11, 1.21, 1.48, and 3.43 times the initial permeability K_0 , respectively. The order of permeability values at differential water pressure of 14 MPa and confining pressure of 17 MPa is: $K_{min} < K_c < K_0 < K_z < K_s < K_{max}$.

From Table 2, it can be observed that, for fractured limestone specimens, the ratio of K_{max} to K_{min} falls in the range of 4–20 and the ratio of K_s to K_{min} is between 1.5 and 6.0. The results are close to the experimental observations from Li et al. (1994, 1995), who studied the permeability characteristics of Yinzhuang sandstone in complete stress–strain process. It has been found by Li et al. (1994, 1995) that the ratio between the highest and lowest permeability varies with a general range of 10–20, and the range of the ratio between the permeability of the peak stress and the lowest permeability is 1.123–12.31. It is noted that all of the six key permeability values mentioned above follow increasing tendency with the increase in differential water pressure at the same confining pressure on a whole. For example, at confining pressure $p_c = 17$ MPa, the ratio values of initial permeability at $\Delta p_w = 2$ and 8–14 MPa are 13.0 and 37.0%, respectively. The ratio values mentioned above are 20.2 and 44.5% for the permeability at peak strength point and 28.1 and 60.4% for the maximum permeability, respectively. It indicates that under the same stress state, with the higher differential water pressure, the six key permeability values are greater.

The effect of confining pressure on permeability was observed in Table 2. At the same differential water pressure, all permeability values decrease nonlinearly with the increasing confining pressure. For example, at $\Delta p_w = 2$ MPa, the ratio values of the initial permeability at $p_c = 7, 12$ and 17–22 MPa are 3.52, 2.37, and 1.26, respectively.

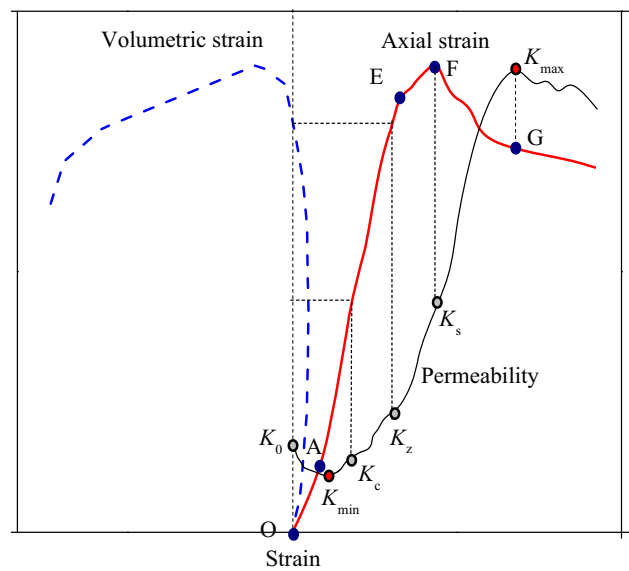


Fig. 11 Representative permeability–axial and volumetric strains curves in complete stress–strain process

The ratio values mentioned above are 2.02, 1.70, and 1.13 for the permeability at peak strength point and 1.58, 1.79, and 1.09 for the maximum permeability as well.

Relationship between permeability and volumetric strain

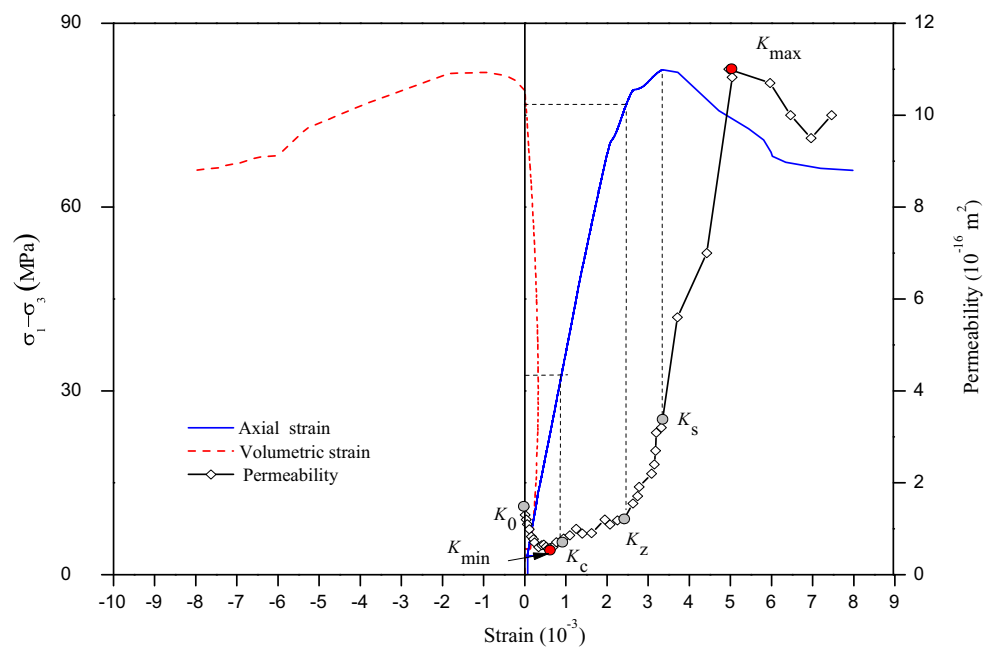
The permeability evolution during triaxial deformation is clearly linked to change in volumetric strain as illustrated in the plots for permeability vs volumetric strain (Figs. 15, 16, 17).

As shown in Fig. 15, at differential water pressure of 2 MPa and confining pressure of 17 MPa, the stage of permeability drop corresponds to the volumetric compression phase. The minimum permeability, K_{min} , corresponding to where the volumetric strain is 3.28×10^{-4} , is very close to the permeability K_c of the maximum volumetric strain ($\epsilon_{vmax} = 3.37 \times 10^{-4}$). Beyond the minimum permeability point, i.e., nearby onset of dilatancy, the permeability evolution starts to move from decrease to increase. An obvious increase in permeability shows up, accompanied with the volumetric dilation. A jump of permeability shows up just after peak strength is reached. The drastic dilatancy of volumetric strain at post-peak stage results in a rapid increase of permeability till the maximum permeability is reached, and the permeability follows a decay trend with some small fluctuations at residual strength stage afterward. Thus, the evolution of permeability is closely correlated with the volumetric strain at relatively lower differential water pressure. It is noted that at differential water pressure of 5 MPa, the relationship between permeability and volumetric strain also follows the rules above. The result is in good agreement

Table 2 Six key permeability values in complete stress–strain process

Δp_w (MPa)	p_c (MPa)	K_0 (10^{-16} m ²)	K_{min} (10^{-16} m ²)	K_c (10^{-16} m ²)	K_z (10^{-16} m ²)	K_s (10^{-16} m ²)	K_{max} (10^{-16} m ²)
2	7	4.12	2.46	2.87	3.80	6.03	15.8
	12	2.78	1.25	1.79	3.41	5.09	17.9
	17	1.47	0.601	0.710	1.20	3.37	10.9
	22	1.17	0.51	0.84	1.05	2.99	10.0
5	7	8.60	6.06	7.78	8.64	10.64	22.1
	12	4.78	3.14	3.67	5.19	8.31	12.9
	17	3.09	2.10	4.05	4.10	9.18	13.7
	22	1.89	1.65	1.77	2.58	6.01	9.22
8	12	5.65	3.65	6.07	7.13	11.4	27.8
	17	4.18	2.47	3.39	5.64	7.61	23.6
	22	3.82	2.60	3.99	3.54	7.89	25.0
11	12	10.1	8.02	9.89	12.1	17.9	44.0
	17	7.76	5.14	7.84	9.10	14.8	23.7
	22	6.13	4.76	7.79	9.25	13.0	18.6
14	17	11.3	10.6	12.5	13.7	16.7	38.8
	22	7.51	5.70	8.92	15.0	16.1	29.8

Fig. 12 Permeability–strain curves in complete stress–strain process at $p_c = 17$ MPa and $\Delta p_w = 2$ MPa



with the experimental observation from Heiland (2003). It was found from Heiland (2003) that for most rock specimens, as long as compression is the dominating mechanism as indicated by positive volumetric strain, permeability of rock decreases and, however, permeability starts to increase accompanied with the onset of dilatancy.

For the differential water pressures of 8–14 MPa, the stage of volumetric compression imperfectly corresponds to the stage of permeability drop. The stage of permeability drop is shorter than that of volumetric compression as

shown in Figs. 16 and 17. There is a contradictory stage (i.e., the volumetric strain range of 3.61×10^{-4} – 4.52×10^{-4} for $\Delta p_w = 8$ MPa, and 1.39×10^{-4} – 6.91×10^{-4} for $\Delta p_w = 14$ MPa), where the volumetric compression is compressed, while the permeability increases at the differential water pressures of 8 and 14 MPa. It is interesting to note that, at differential water pressure of 14 MPa, the stage of permeability drop is insignificant. It indicates that for the fractured limestone subjected to relatively higher pore fluid pressure, the local

Fig. 13 Permeability–strain curves in complete stress–strain process at $p_c = 17$ MPa and $\Delta p_w = 8$ MPa

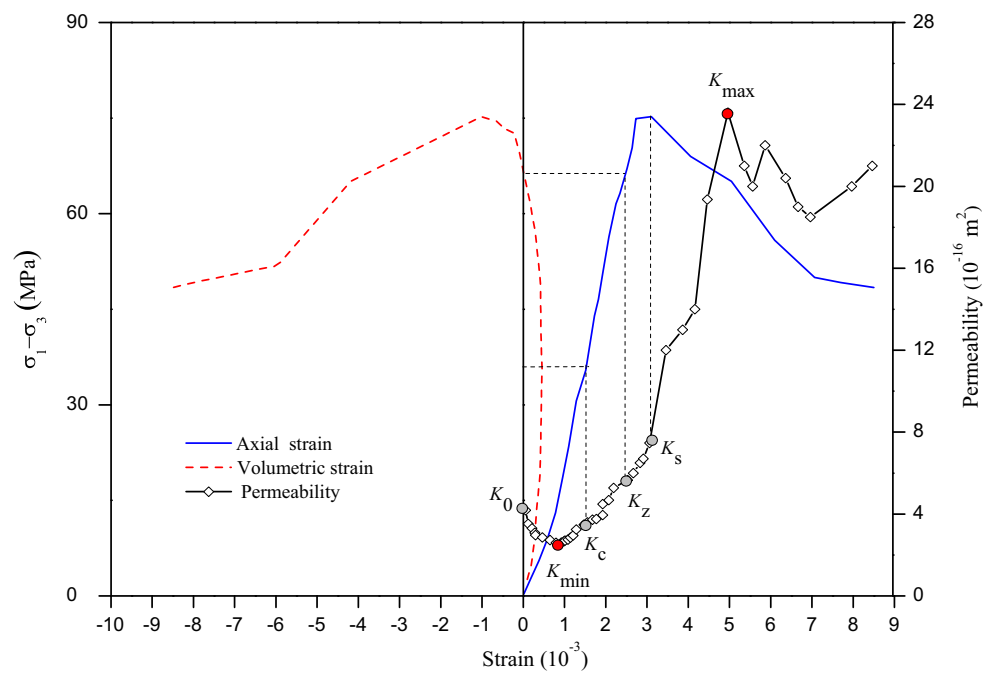
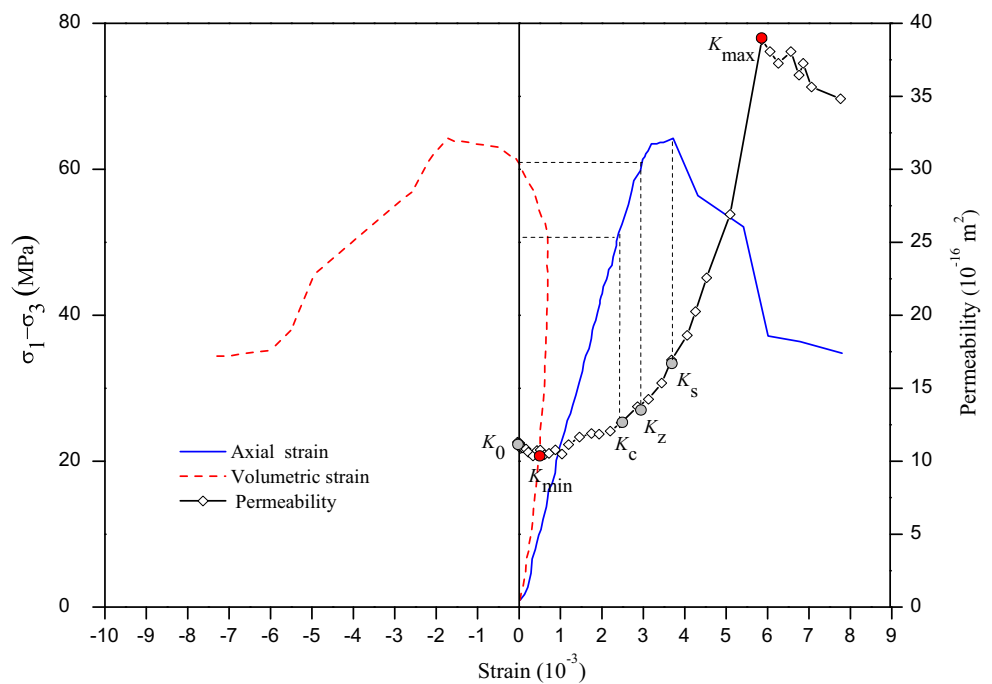


Fig. 14 Permeability–strain curves in complete stress–strain process at $p_c = 17$ MPa and $\Delta p_w = 14$ MPa



hydraulic fractures which result in the increase in permeability may occur at the stage of volumetric compression.

The permeability change laws at the stages of volumetric compression and dilatancy at differential water pressures 2, 8, and 14 MPa under confining pressure 17 MPa were plotted in Fig. 18a, b, respectively. The

results were normalized (i.e., K/K_0 was adopted) in Fig. 18a.

For the stage of volumetric compression, a cubic polynomial can be used to describe the relationship between permeability and volumetric strain

$$K_y/K_0 = \alpha \epsilon_v^3 + \eta \epsilon_v^2 + \gamma \epsilon_v + 1 \quad (\epsilon_v \leq \epsilon_c) \tag{11}$$

Fig. 15 Permeability–volumetric strain curves in complete stress–strain process at $p_c = 17$ MPa and $\Delta p_w = 2$ MPa

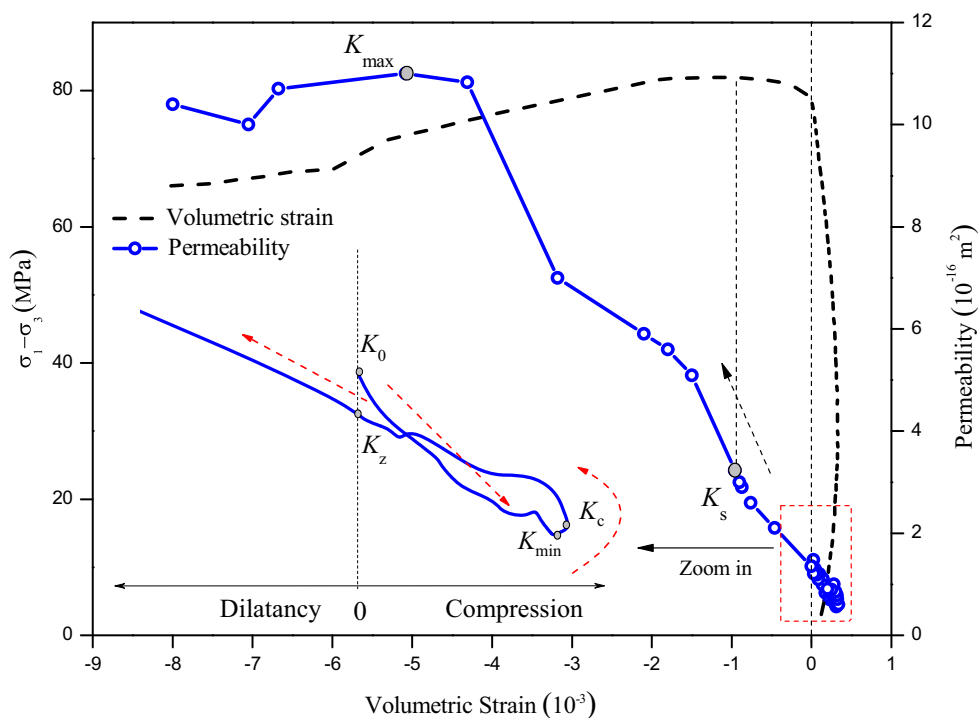
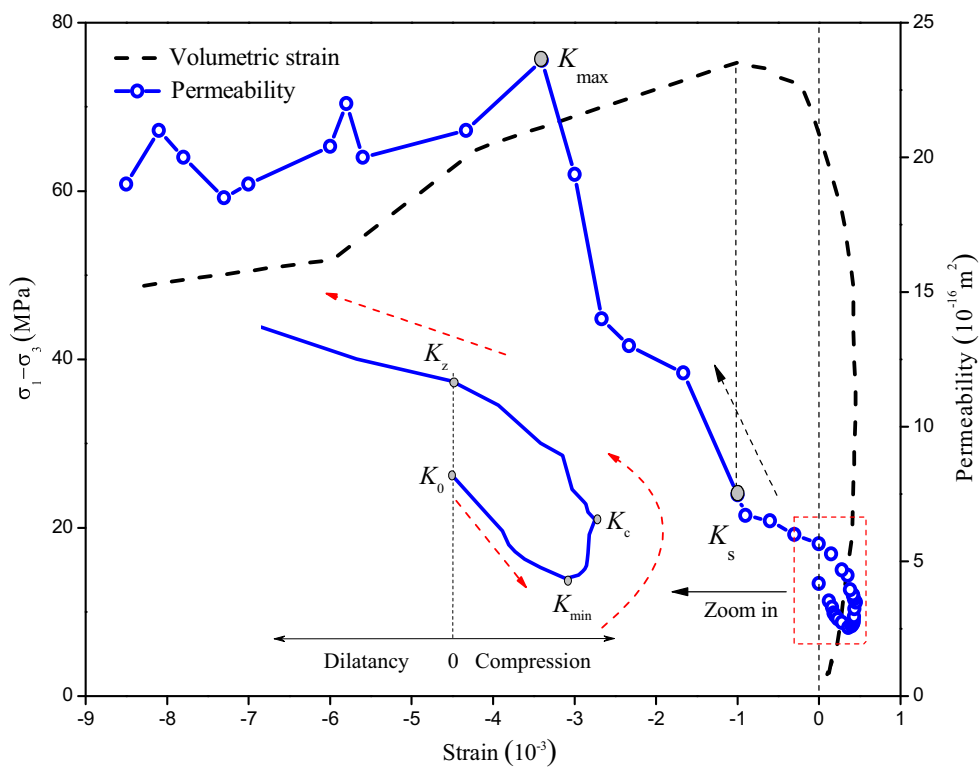


Fig. 16 Permeability–volumetric strain curves in complete stress–strain process at $p_c = 17$ MPa and $\Delta p_w = 8$ MPa

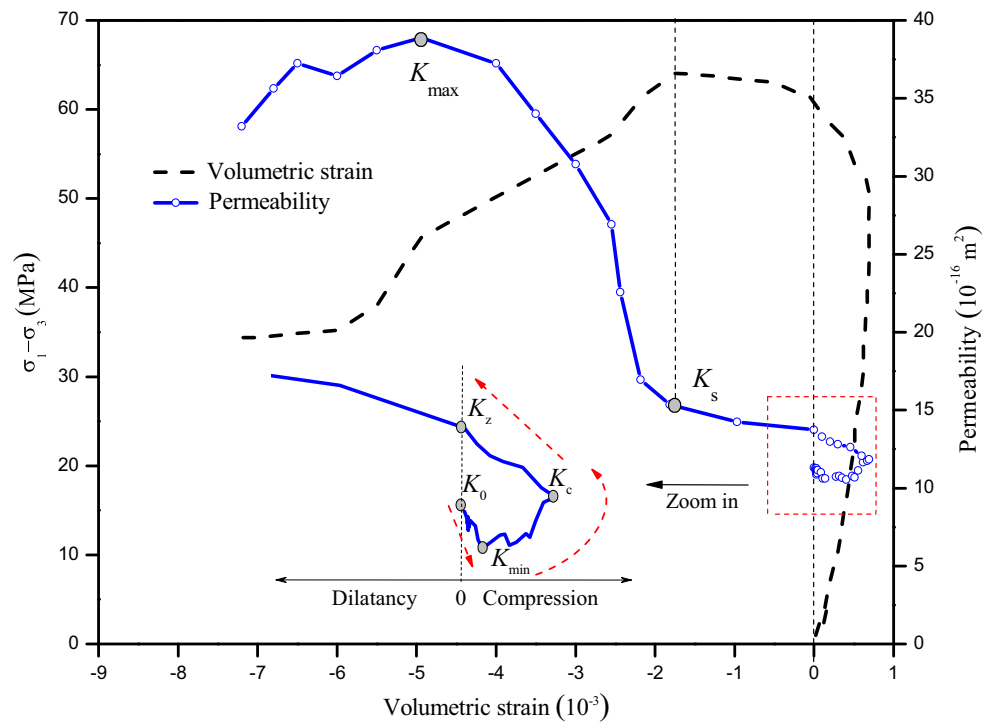


where α , η and γ are fitting parameters. The fitting curves at the differential water pressures of 2, 8, and 14 MPa were all plotted in Fig. 18a, and the fitting parameters were listed Table 3. The fitting curves are in good agreement

with experimental data with an average correlation coefficient R^2 above 0.9.

For fractured limestone specimens, Eq. (11) can describe not only the trend of monotonous permeability drop at the low differential water pressures of 2–5 MPa,

Fig. 17 Permeability–volumetric strain curves in complete stress–strain process at $p_c = 17$ MPa and $\Delta p_w = 14$ MPa



but also the trend of the decrease firstly, and then increase in permeability at the high differential water pressures of 8–14 MPa. In Eq. (11), the permeability is a function of volumetric strain, instead of a constant value. It will certainly be believed that the analysis results should be more applicable and more coincident with practice if both the common constitutive equations and the permeability–volumetric strain equations [Eq. (11)] are accepted simultaneously to form the governing equations.

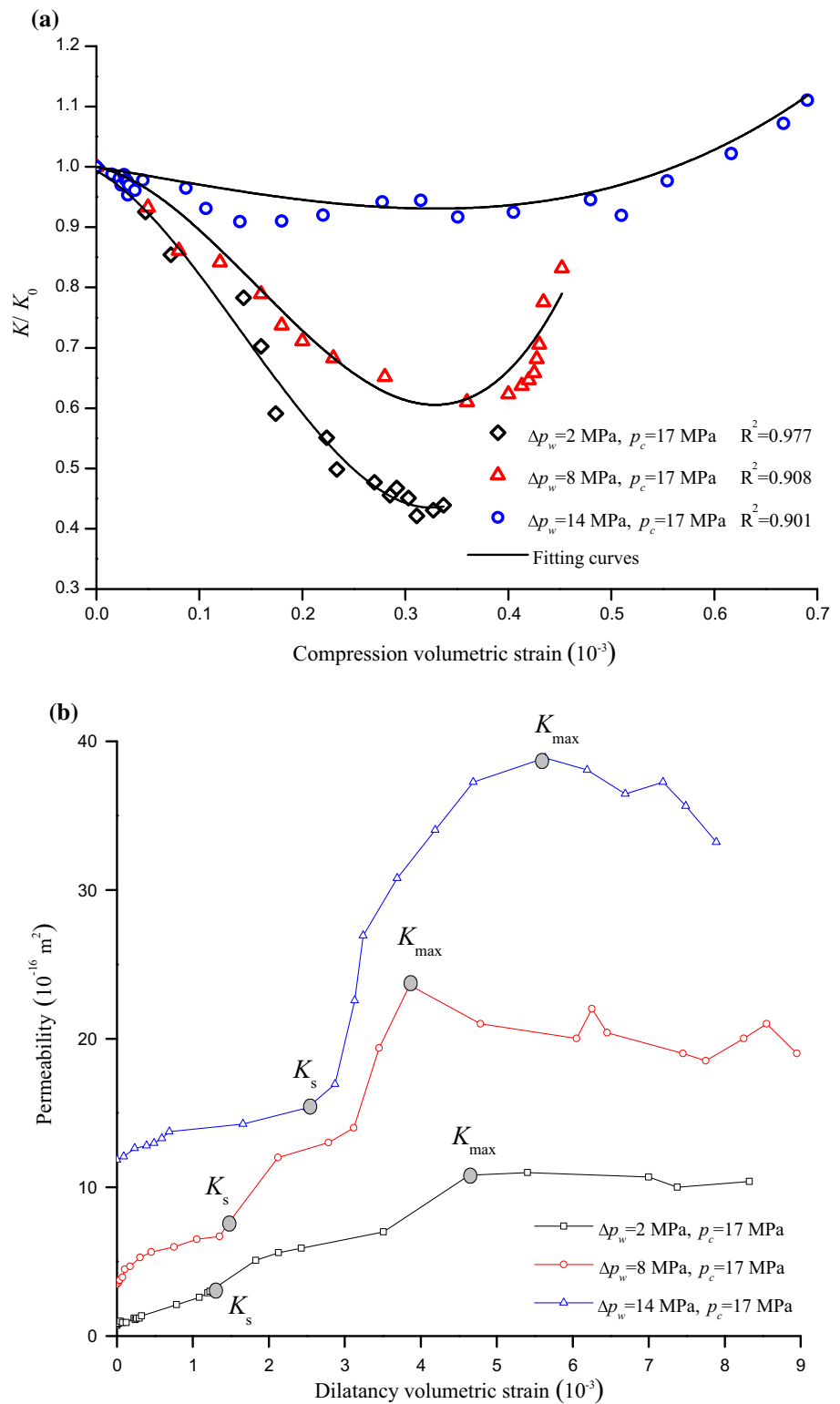
The permeability increases with volumetric dilatancy, while a small reduction occurs at residual strength stage. Figure 18b shows the relationship between permeability and volumetric dilatancy. The different evolution laws at various differential water pressures are observed. At a differential water pressure of 2 MPa, the permeability approximately increases linearly at volumetric dilatancy stage, neglecting the reduction in permeability at residual strength stage, which is in agreement with the experimental observation from Heiland (2003). However, at differential water pressures of 8 and 14 MPa, the permeability firstly increases gradually and then rises rapidly to maximum value beyond peak strength at the dilatant stage. At volumetric dilatancy stage, the permeability is sensitive to cracks development. Due to the polytropic and randomness of cracks development at the dilatancy stage, the permeability–volumetric strain curve is very complex. Therefore, it is very difficult and inappropriate to describe the relationship between the permeability and volumetric strain by a uniform fitting equation at the dilatancy stage.

Conclusions

To clarify mechanical and permeability characteristics of fractured limestone in complete stress–strain process under hydromechanical coupling condition, the hydromechanical coupling tests on fractured limestone at various differential water pressures and confining pressures were performed, based on focusing on the relationship between permeability and complete stress–strain curve.

1. The mechanical characteristics of fractured limestone specimens are sensitive to the confining pressure, differential water pressure, and the effective minimum principal stress. The peak strength, residual strength, and deformation modulus increase with the increasing confining pressure on a whole. The increasing differential water pressure weakens rock strength and deformation modulus, by activating the lateral deformation of fractured limestone, which is attributed to the decrease in the effective minimum principal stress. The experimental results confirm the validity of Mohr–Coulomb yield criterion, considering the effective stress effect under hydromechanical coupling condition.
2. The permeability values display four stages of decrease–gradual increase–rapid increase–small drop in complete stress–strain process. These four stages roughly correspond to volumetric compression stage, elastic deformation stage, yield, post-peak stage, and residual strength, respectively. At relatively lower

Fig. 18 Permeability–volumetric strain curves at **a** compression and **b** dilatancy stages



differential water pressure of 2–5 MPa, the correspondence above is perfect. However, at relatively higher differential water pressures of 8–14 MPa, permeability reduction stage is shorter than the stage of volumetric compression.

3. The six key permeability values are selected from the experimental data to study permeability evolution laws. At relatively lower differential water pressure of 2 MPa, $K_{min} \approx K_c < K_z < K_0 < K_s < K_{max}$. However, at relatively higher differential water pressures of

Table 3 Fitting parameters

p_c (MPa)	Δp_w (MPa)	α	η	γ	R^2
17	2	23.4	-9.93	-0.961	0.977
17	8	18.4	-8.53	-0.356	0.908
17	14	0.882	0.162	-0.371	0.901

8 and 14 MPa, $K_{min} < K_c < K_0 < K_z < K_s < K_{max}$. The six key permeability values rise with the increase in differential water pressure at the same confining pressure, while they reduce with increasing confining pressure at the same differential water pressure on a whole.

- A cubic polynomial can be used to describe the relationship between permeability and volumetric strain at volumetric compression stage. It is difficult and inappropriate to describe the relationship between the permeability and volumetric strain by a uniform fitting equation due to the complicated permeability–volumetric strain curve patterns at the dilatancy stage.
- The permeability of fractured rock is a variable quantity dependent on the development of stress and strain. The maximum permeability of rock usually appears during the strain-softening stage, rather than in coincidence with its peak strength.

Acknowledgements This research is supported by the National Natural Science Foundation of China (51274097, 51434006, 51604299, 41274126); the Scientific Research Fund of Hunan Provincial Education Department (13A020); the Natural Science Foundation of Hunan province (2015JJ2067); the Open Projects of State Key Laboratory of Coal Resources and Safe Mining (SKLRCRSM16KF12).

References

Bai M, Meng F, Elsworth D, Roegiers JC (1999) Analysis of stress dependent permeability in nonorthogonal flow and deformation fields. *Rock Mech Rock Eng* 32:195–219

Barton N, Bandis S, Bakhtar K (1985) Strength, deformation and conductivity coupling of rock joints. *Int J Rock Mech Min Sci Geomech Abstr* 22:121–140

Baud P, Schubnel P, Wong T (2000) Dilatancy, compaction and failure mode in solnhofen limestone. *J Geophys Res* 105(B8):289–303

David C, Menendez B, Zhu W, Wong TF (2001) Mechanical compaction, microstructures and permeability evolution in sandstones. *Phys Chem Earth A* 26:1–2:45–51

Gangim AF (1978) Variation of whole and fractured porous rock permeability with confining pressure. *Int J Rock Mech Min Sci Geomech Abstr* 15:249–257

Ghabezloo S, Sulem J, Guédon S, Martineau F (2009) Effective stress law for the permeability of a limestone. *Int J Rock Mech Min Sci* 46:297–306

Heiland J (2003) Laboratory testing of coupled hydromechanical processes during rock deformation. *Hydrogeol J* 11:122–141

Hicks TW, Pine RJ, Willis Richards J (1996) A hydro-thermo-mechanical numerical model for HDR geothermal reservoir evaluation. *Int J Rock Mech Min Sci Geomech Abstr* 33:499–511

Hubbert M, Rubey W (1959) Role of fluid pressure in mechanics of overthrust faulting. *Geol Soc Am* 70:115–166

Jaeger JC, Cook NGW (1979) *Fundamentals of rock mechanics*, 3rd edn. Chapman & Hall, London

Konecny P, Kozusnikova A (2011) Influence of stress on the permeability of coal and sedimentary rocks of the Upper Silesian basin. *Int J Rock Mech Min Sci* 48:347–352

Lajtai EZ, Schmidtke RH, Bielius LP (1987) The effect of water on the time-dependent deformation and fracture of a granite. *Int J Rock Mech Min Sci Geomech Abstr* 24:247–255

Laloui L, Nuth M (2009) On the use of the generalised effective stress in the constitutive modelling of unsaturated soils. *Comput Geotech* 36:20–23

Li SP, Li YS, Wu ZY (1994) Permeability-strain equations corresponding to the complete stress–strain path of Yinzhuang sandstone. *Int J Rock Mech Min Sci Geomech Abstr* 31:383–391

Li SP, Li YS, Wu ZY (1995) The permeability-strain equations relating to the complete stress–strain path of the rock. *Chin J Geotech Eng* 17:13–19 (**In Chinese**)

Li SP, Wu DX, Xie WH, Li YS, Wu ZY, Zhou G, Zhao HY (1997) Effect of confining pressure, pore pressure and specimen dimension on permeability of Yinzhuang sandstone. *Int J Rock Mech Min Sci* 34:175

Li JW, Xu J, Wang L, Yang HT, Yang ZY (2013) Water–rock coupling test on mechanical properties of sandy slate rock mass. *Chin J Geotech Eng* 24:247–255 (**in Chinese**)

Li Y, Chen YF, Zhou CB (2016) Effective stress principle for partially saturated rock fractures. *Rock Mech Rock Eng* 49:1091–1096

Martin JB, Chandler NA (1994) The progressive fracture of Lac du Bonnet granite. *Int J Rock Mech Min Sci Geomech Abstr* 31:643–659

Masuda K (2001) Effect of water on rock strength in a brittle regime. *J Struct Geol* 23:1653–1657

Meng L, Li T, Xu J, Chen G, Ma H, Yin H (2012) Deformation and failure mechanism of phyllite under the effects of THM coupling and unloading. *J Mt Sci* 9:788–797

Olivella S, Gens A, Gonzalez C (2004) THM analysis of a heating test in a fractured tuff. *Elsevier Geo-Engineering Book Series: coupled thermo–hydro–mechanical–chemical processes in geosystems-fundamentals. Model Exp Appl* 2:181–186

Rutter E (1986) On the nomenclature of mode of failure transitions in rocks. *Tectonophysics* 12:381–387

Schulze O, Popp T, Kern H (2001) Development of damage and permeability in deforming rock salt. *Eng Geol* 61:163–180

Shan RL, Jiang YS, Li BQ (2000) Obtaining dynamic complete stress-strain curves for rock using the split Hopkinson pressure bar technique. *Int J Rock Mech Min Sci* 37:983–992

Shao JF, Zhou H, Chau KT (2005) Coupling between anisotropic damage and permeability variation in brittle rocks. *Int J Numer Anal Methods Geomech* 29:1231–1247

Suri P, Azeemuddin M, Zaman M, Kukreti AR, Roegiers JC (1997) Stress dependent permeability measurement using the oscillating pulse technique. *J Petrol Sci Eng* 17:247–264

Tsang YW, Witherspoon PA (1981) Hydro mechanical behavior of a deformable rock fracture subject to normal stress. *J Geophys Res* 86(B10):9187–9298

Tuncay K, Corapcioglu MY (1995) Effective stress principle for saturated fractured porous media. *Water Resour Res* 31:3103–3106

- Vásárhelyia B, Ván P (2006) Influence of water content on the strength of rock. *Eng Geol* 84:70–74
- Von Terzaghi K (1923) Die Berechnung der Durchlässigkeit des Tones aus dem Verlauf der hydrodynamischen Spannungsercheinungen, *Sitzungsber Akad Wiss, Math-Naturwiss Kl, Abt. IIa* 132:125–138
- Wang JA, Park HD (2002) Fluid permeability of sedimentary rocks in a complete stress–strain process. *Eng Geol* 63:291–300
- Wang HL, Xu WY (2013) Relationship between permeability and strain of sandstone during the process of deformation and failure. *Geotech Geolog Eng* 31:347–353
- Wang SY, Sloan SW, Fityus SG, Griffiths DV, Tang CA (2013) Numerical modeling of pore pressure influence on fracture evolution in brittle heterogeneous rocks. *Rock Mech Rock Eng* 46:1165–1182
- Xie SY, Shao JF (2015) An experimental study and constitutive modeling of saturated porous rocks. *Rock Mech Rock Eng* 48:223–234
- Zhang J, Standifird WB, Roegiers JC, Zhang Y (2007) Stress dependent fluid flow and permeability in fractured media: from lab experiments to engineering applications. *Rock Mech Rock Eng* 40:13–21
- Zhang R, Jiang Z, Sun Q, Zhu S (2013) The relationship between the deformation mechanism and permeability on brittle rock. *Nat Hazards* 66:1179–1187
- Zhu W, Wong T (1997) The transition from brittle faulting to cataclastic flow: permeability evolution. *J Geophys Res* 102:3027–3041
- Zoback MD, Byerlee JD (1975) The effect of microcrack dilatancy on the permeability of Westerly granite. *J Geophys Res* 80:752–755